Raman Lidar Measurements during the International H_2O Project. Part II: Case Studies

D. N. WHITEMAN,* B. DEMOZ,* P. DI GIROLAMO,+ J. COMER,# I. VESELOVSKII,@ K. EVANS,@ Z. WANG,& D. SABATINO,+ G. SCHWEMMER,* B. GENTRY,* R-F. LIN,@ A. BEHRENDT,** V. WULFMEYER,** E. BROWELL,++ R. FERRARE,++ S. ISMAIL,++ AND J. WANG##

*NASA GSFC, Greenbelt, Maryland
+ DIFA, University of Basilicata, Potenza, Italy
# Science Systems Applications, Inc., Lanham, Maryland
@ University of Maryland, Baltimore County, Baltimore, Maryland
& University of Wyoming, Laramie, Wyoming
** University of Hohenheim, Hohenheim, Germany
++ NASA Langley Research Center, Langley, Virginia
National Center for Atmospheric Research, Boulder, Colorado

(Manuscript received 23 March 2005, in final form 14 July 2005)

ABSTRACT

The NASA GSFC Scanning Raman Lidar (SRL) participated in the International H_2O Project (IHOP) that occurred in May and June 2002 in the midwestern part of the United States. The SRL system configuration and methods of data analysis were described in Part I of this paper. In this second part, comparisons of SRL water vapor measurements and those of Lidar Atmospheric Sensing Experiment (LASE) airborne water vapor lidar and chilled-mirror radiosonde are performed. Two case studies are then presented: one for daytime and one for nighttime. The daytime case study is of a convectively driven boundary layer event and is used to characterize the daytime SRL water vapor random error characteristics. The nighttime case study is of a thunderstorm-generated cirrus cloud case that is studied in its meteorological context. Upper-tropospheric humidification due to precipitation from the cirrus cloud is quantified as is the cirrus cloud optical depth, extinction-to-backscatter ratio, ice water content, cirrus particle size, and both particle and volume depolarization ratios. A stability and back-trajectory analysis is performed to study the origin of wave activity in one of the cloud layers. These unprecedented cirrus cloud measurements are being used in a cirrus cloud modeling study.

1. Introduction

The International H_2O Project (IHOP), which occurred in the Midwestern United States between 13 May and 25 June 2002, was the largest meteorological field campaign ever held in the United States (Weckwerth et al. 2004). The instrumentation used during IHOP included seven research aircraft carrying three water vapor lidars and one wind lidar, mobile radar systems for storm chasing, and a ground-based site in the western panhandle of Oklahoma that included the National Aeronautics and Space Administration (NASA) Goddard Space Flight Center (GSFC) Scanning Raman Lidar (SRL). The goal of IHOP was to improve forecasting of convective storm systems and precipitation. The first part of this paper (Whiteman et al. 2006, hereafter referred to as Part I) focused on the instrumentation of the SRL during IHOP and the data analysis technique used. In Part II, comparisons of SRL water vapor measurements with other instruments are presented followed by daytime and nighttime case studies that permit the error characteristics of the system to be quantified and illustrate the diurnal measurement capabilities.

2. SRL operations during IHOP

During the first several days of IHOP, numerous instruments including the SRL were not fully operational, thus delaying the effective onset of the experiment.

Corresponding author address: D. N. Whiteman, NASA GSFC, Code 613.1, Building 33, Room D404, Greenbelt, MD 20771.
E-mail: david.n.whiteman@nasa.gov

© 2006 American Meteorological Society

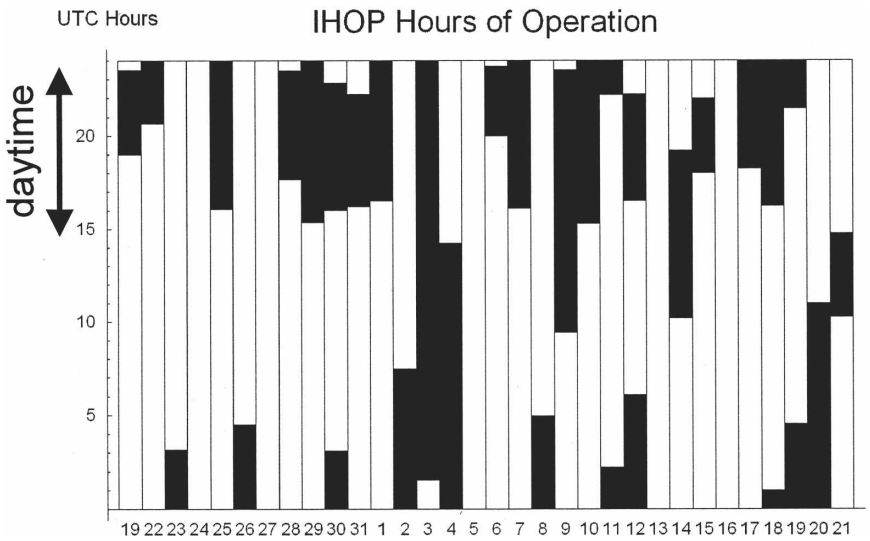

FIG. 1. The SRL hours of operation as a function of day during IHOP beginning on 19 May and ending on 21 Jun. Most measurements were concentrated during the daytime when convection was most likely to develop. Several early morning low-level jet experiments also were performed.

Once operations began in earnest, a total of approximately 225 h of vertically pointing SRL data were acquired during IHOP. A chart of the operational periods of the SRL during IHOP is shown in Fig. 1. Most of the measurements were concentrated during late morning to early evening hours when convection was most likely to develop. There were several early morning jet experiments that also took place. A complete listing of the IHOP measurement periods and objectives can be seen online at http://www.ofps.ucar.edu/ihop/catalog/missions.html.

3. Comparison of SRL water vapor measurements with other sensors

Atmospheric water vapor measurements were acquired by the ground-based SRL, the airborne Lidar Atmospheric Sensing Experiment (LASE) system (Browell and Ismail 1995; Browell et al. 1997), and the National Center for Atmospheric Research (NCAR) reference sonde [SnowWhite (SW)] (Wang et al. 2003) during IHOP. Example and mean comparisons of SRL and these other profilers are presented next. These comparisons differ from earlier preliminary analysis (Sabatino et al. 2004) in that they use the final SRL data analysis.

The standard analysis of the SRL water vapor mixing ratio data from IHOP used moving-window averages in the vertical and temporal domains. The temporal averaging window for the water vapor data was 3 min while the spatial averaging windows were as follows: 0–1 km: 90 m, l–2 km: 150 m, 2–3 km: 210 m, 3–4 km: 270 m, >4 km: 330 m. The resulting water vapor temporal resolutions, determined by the half-power point in a Fourier spectral analysis, is approximately 2 min while the vertical resolution varies approximately as follows: 0–1 km: 60 m, 1–2 km: 100 m, 2–3 km: 150 m, 3–4 km: 180 m, >4 km: 210 m.

a. LASE

Comparison of SRL and LASE water vapor data was possible on four distinct days: 30 May, 3 June, 9 June, and 14 June 2002. Only those cases characterized by distances smaller than 2.5 km between the closest point of LASE overpass and Homestead were considered. This provided a total of 24 possible comparisons between SRL and LASE. However, comparisons for 14 June were discarded because of an operational problem with LASE that precluded an independent comparison with SRL. For this reason, the number of comparisons considered here is 11. The vertical resolution of the LASE data was 330 m while the effective vertical resolution of the SRL data varied between 60 and 210 m. Comparisons are based on 1-min averaging of LASE data and a variable temporal averaging of SRL data that increases with height. A variable temporal average with height is an attractive way to process data from ground-based lidar systems since the signals decrease with altitude due both to the natural range-squared decrease of optical signals as well as the decrease in num-

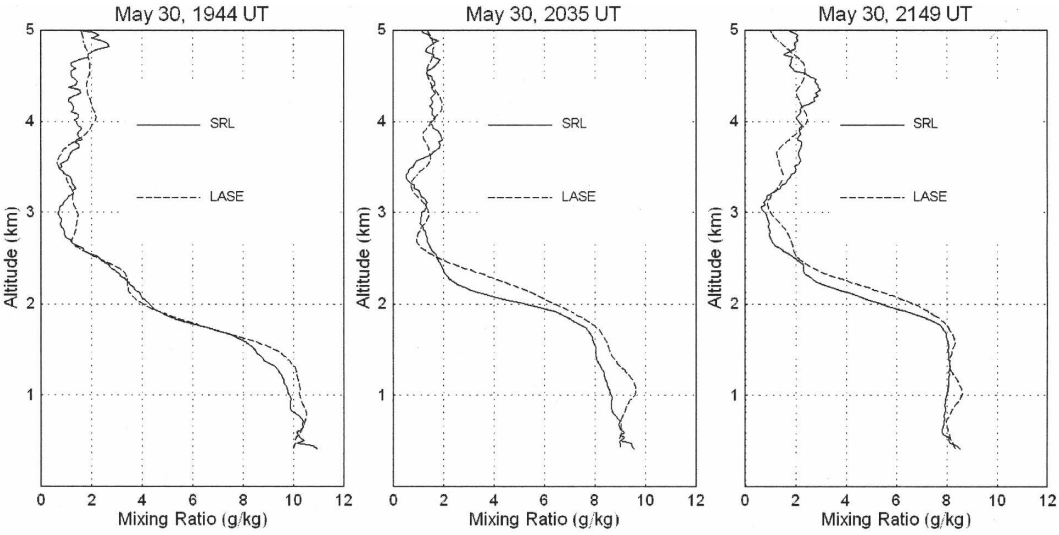

FIG. 2. Example comparisons of three overflights of the SRL site by the LASE airborne water vapor lidar on 30 May 2002. The SRL and LASE data use 10- and 1-min averages, respectively. Note that all profiles are acquired in the daytime.

ber density of water vapor, particularly above the boundary layer. An airborne lidar system that looks downward has the advantage that the range-squared signal decrease is compensated for by the increasing number density of scatterers that is typically present when progressing to lower altitudes (Whiteman et al. 2001b). Variable temporal smoothing of the upward-looking lidar data can result in an average profile that possesses similar random error as a function of altitude, permitting more accurate comparisons with an airborne lidar looking downward. In these comparisons, therefore, the number of profiles used in the SRL water vapor analysis varies from 1 at the lowest altitudes to 11 above the boundary layer, with the goal of maintaining random error of 10% or less at all altitudes. This technique is described in more detail in the context of the upper-tropospheric water vapor measurements described later in section 4b(3).

Comparisons between SRL and LASE are shown for three overpasses on 30 May in Fig. 2. The measurements of the two lidars show good general agreement for these bright daytime measurements. Larger deviations between the two instruments are occasionally found at the top of the boundary layer, where the effect of spatial inhomogeneities (as manifested by dry air mixing down from above the boundary layer) may be larger. When the daytime sky is particularly bright, such as under hazy conditions, random errors for a ground-based Raman water vapor lidar rise more quickly above the boundary layer [see section 4a(1) for more discussion of the SRL random error characteristics]. To permit a mean assessment of SRL and LASE above the boundary layer, therefore, some filtering of the data was required. The profiles of both LASE and SRL were filtered by rejecting mixing ratio values either below 0 or above vapor saturation or when the random error exceeded 100% and then block averaged to 250-m vertical resolution. Any blocks of 250 m that had data removed due to this filtering were not used in the comparison analysis of the two systems. One of the effects of this filtering was to reject some of the comparisons above the boundary layer under the brightest of daytime conditions. The mean comparison of SRL and LASE profiles using this filtering technique is shown on the left of Fig. 3. The normalized differences calculated after this filtering technique and shown on the right of Fig. 3 indicate that the mean profiles agree generally within ±20% up to 5 km. The error bars shown provide the standard deviation of the normalized differences of the block-averaged results. Both atmospheric variation (due to the horizontal averaging of airborne LASE but not ground-based SRL) and instrument-to-instrument variation are contributing to the differences observed here. The integrated precipitable water of the mean profiles displayed in Fig. 3 were compared over the altitude range of 0.6 and 5.0 km with the result that the LASE PW was on average 2.7% higher than the SRL.

b. NCAR reference sonde

Comparisons between SRL and the NCAR reference sonde, which combines a SnowWhite chilled-mirror sensor and a Vaisala RS-80 radiosonde (Wang et al. 2004), have been also performed. Four distinct sonde launches were considered on 28 May, 9 June, 18 June,

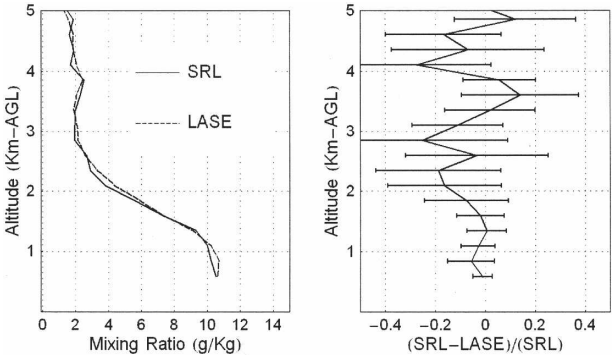

FIG. 3. Mean profile and normalized difference comparisons between SRL and LASE during the IHOP experiment based on 11 separate overpasses. In general the mean profiles agree within ±20% over the altitude range displayed. The integrated precipitable water between 0.5 and 5.0 km of the mean LASE profile is 2.6% higher than the corresponding SRL profile. See text for more details.

and 20 June 2002. The same data filtering and noise rejection techniques described above were used in this comparison as well. Water vapor mixing ratios for the reference sonde have been calculated using pressure information from simultaneous Vaisala RS80 radiosondes since pressure information from the reference sonde itself was considered to not be reliable. Figure 4 shows the mean profile and normalized differences of SRL and the reference sonde. The profiles show good general agreement with normalized differences generally less than 10% to an altitude of 5 km. The error bars shown provide the standard deviation of the normalized differences of the block-averaged results. Data points that lack error bars indicate that there was only one profile comparison at those altitudes. The integrated precipitable from 0.6 to 5.0 km was 1.5% less in the reference sonde than in the SRL.

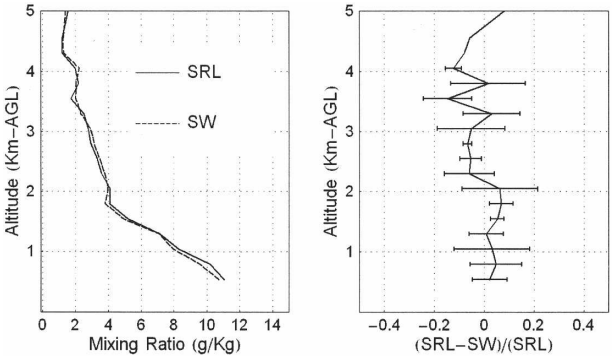

FIG. 4. Mean profile and normalized difference comparisons between the SRL and the NCAR reference sensor that includes SnowWhite (SW) and Vaisala RS-80H. In general the profiles agree within ±10% over the altitude range displayed. The integrated precipitable water between 0.4 and 5.0 km of the mean SRL profile was 1.5% higher than that of the reference sonde.

In general the comparison of the SRL with the reference sonde shows lower variability than that with LASE. This result is believed to reflect the greater effect of horizontal variation in the atmosphere that will influence comparisons of airborne and ground-based lidar systems. Also, the LASE–SRL comparisons use a larger percentage of daytime cases than the reference sonde comparisons. Therefore, convective variation and random noise due to increased solar background are both expected to be higher in these comparisons.

4. Daytime and nighttime case studies

The challenge for Raman lidar measurements is particularly large during the daytime when the large solar background makes accurate measurement of the relatively weak Raman signals more difficult. Therefore the measurement characteristics of a non-solar-blind water vapor Raman lidar will differ considerably between daytime and nighttime. SRL measurements from two IHOP intensive observation periods will now be presented in order to illustrate the daytime and nighttime measurement capability of the SRL as configured for IHOP.

a. Daytime convective boundary layer measurements

On 22–23 May 2002, the IHOP forecasting team predicted that convection would initiate in the Oklahoma panhandle, near the SRL location. The SRL water vapor mixing ratio measurements from this period are shown in the upper left in Fig. 5. The water vapor mixing ratio data are displayed from 0.3 to 5 km and over a range of mixing ratio values of 0–15 g kg^{-1} for a period of ~6.5 h. On this day, the height of the daytime boundary layer was observed to grow from approximately 2.4 km at 2030 UTC to ~3.5 km at 2400 UTC. The dryline moved westward and passed over Homestead at approximately 2230–2245 UTC, as confirmed by radar and other surface measurements. Sunset occurred at approximately 0130 UTC on 23 May (indicated as 2530 UTC in the figure) after which time stronger advection of moist air from the south increased the low-level water vapor mixing ratio values giving rise to the moist low-level air capped by dry air above 1.5 km observed in the figure. The vertical stripes in the water vapor field represent convective plumes of water vapor. The white stripes that extend above the top of the boundary layer at, for example, ~2300 and ~2400 UTC, are due to noise created by the attenuation of the laser beam by convectively generated clouds that formed at the top of the boundary layer. The simulta-

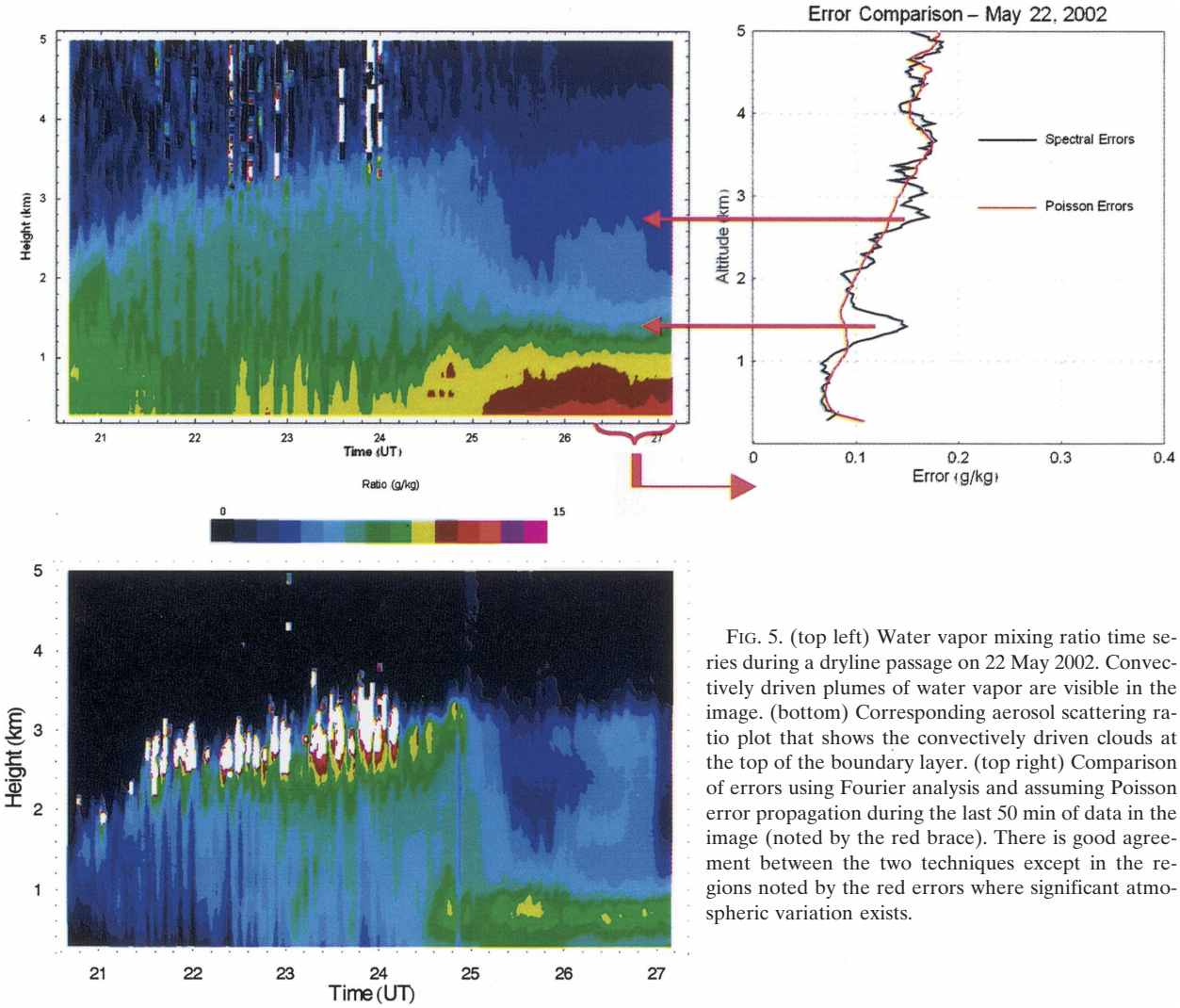

FIG. 5. (top left) Water vapor mixing ratio time series during a dryline passage on 22 May 2002. Convectively driven plumes of water vapor are visible in the image. (bottom) Corresponding aerosol scattering ratio plot that shows the convectively driven clouds at the top of the boundary layer. (top right) Comparison of errors using Fourier analysis and assuming Poisson error propagation during the last 50 min of data in the image (noted by the red brace). There is good agreement between the two techniques except in the regions noted by the red errors where significant atmospheric variation exists.

neously acquired aerosol scattering ratio image is presented in the bottom of Fig. 5 using the same temporal and spatial resolution as in the water vapor mixing ratio image to illustrate the same convective plumes in the aerosol field and to denote the locations of clouds that formed at the top of the boundary layer. For more details on this case, see Demoz et al. (2006).

DAYTIME RANDOM ERROR CHARACTERIZATION

The dryline case of May 22 shown in Fig. 5 has been used to characterize the random errors in the SRL water vapor mixing ratio data. For photon counting data, errors can be calculated assuming Poisson statistics using Eq. (6) from Part I, to be referred to as the water vapor error equation. However, as discussed in Part I, the water vapor mixing ratio measurements in general use a combination of photon-counting and analog measurements. In general, calculating statistics on a single profile of analog data requires that the square of the signal for each laser shot that goes into a summed profile be maintained (Whiteman et al. 1992). That information is not maintained in the current data acquisition electronics so another approach to determining errors in the analog data is required. The method used here is to first convert the analog signal to a virtual count rate scale using the glue coefficients determined through a regression analysis. The virtual count rate corresponding to the analog signal is used for the S terms in the water vapor error equation, and the background determined from the photon-counting data is used for the B terms. The implicit assumption is that the analog data converted to a virtual count rate scale behave according to Poisson statistics.

This method of determining the errors has been tested by comparing the results of the water vapor error equation with errors determined using spectral analysis

techniques where the noise floor in a Fourier power spectrum (Senff et al. 1994; Linné et al. 2000) is determined as a function of height. If a portion of data is used when the atmosphere is stable—that is, where the real atmospheric variation is significantly less than variations introduced by counting statistics—then the noise determined by this Fourier technique can be used to quantify the instrument noise floor. The upper-right panel of Fig. 5 shows the comparison of the Poisson and spectrally determined random errors for the last 50 min of the measurement period (denoted by the horizontal brace on the time axis of the water vapor image). To improve the statistics of this comparison, the data have been used at their raw resolution (1-min temporal and 30-m spatial) instead of the smoothed resolution displayed in the image. In the final 50-min segment of the water vapor mixing ratio image, analog data are used for the water vapor signal between 0.3 and approximately 2.0 km and for the nitrogen signal from 0.3 to 5.5 km. Therefore, the water vapor mixing ratio is calculated using exclusively analog data below approximately 2.0 km for this 50-min segment. Above 2.0 km, the mixing ratio is determined using photon-counting data for the water vapor and analog data for the nitrogen. The plot in Fig. 5 shows that the two methods of determining the variance in the signal agree well except for two altitude ranges between 1.2–1.6 and 2.6–3.2 km, both indicated by horizontal arrows, where the spectrally determined variance exceeds that determined by Poisson statistics. The lower-altitude range corresponds to the top of the nocturnal boundary layer (confirmed by potential temperature analysis from radiosonde) while the upper-altitude range indicates the location of the residual layer. The increased atmospheric variability at these locations leads to larger variance in the spectral quantification of errors since the Fourier technique is quantifying both real atmospheric variation as well as variation due to the counting statistics. Therefore, this example illustrates that the Fourier and Poisson techniques for calculating errors agree well except in regions of increased atmospheric variability, thus supporting the assumption that the technique of calculating errors from the converted analog data assuming Poisson statistics is justified. It also demonstrates that this error comparison technique can be used to discern transition regions in the atmosphere.

The analysis of Fig. 5 validates the use of Poisson statistics to determine the random component of the errors in the water vapor mixing ratio calculation. Figure 6 now presents a comparison of how the errors determined using Poisson statistics varied during the 22–23 May 2002 dataset. Using the smoothed resolution presented in Fig. 5, the random error was calculated at

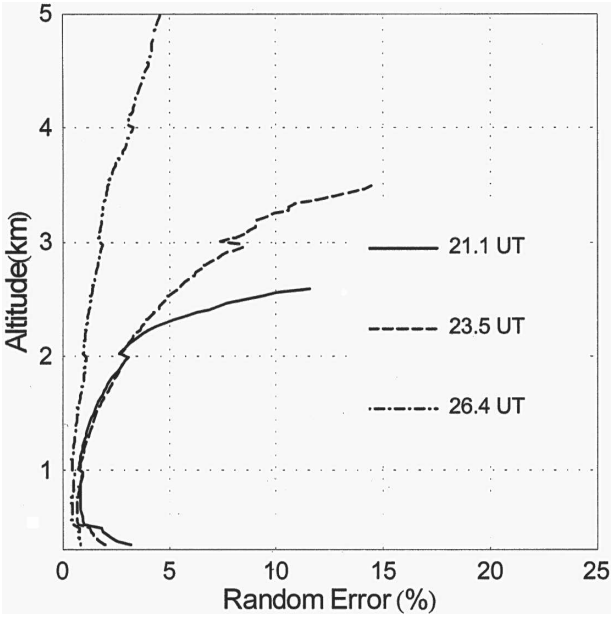

FIG. 6. Random error in the SRL water vapor mixing ratio measurements on 22 May 2002. The random error remains below 10% in the boundary layer using 2-min temporal and 60–200-m spatial resolution.

three times in the dataset: 21.1, 23.5, 26.4 UTC. (The latter time indicates 2.4 UTC on 23 May 2002). The first two of these measurements were in bright daytime conditions while the last was in full darkness. These random error quantifications along with the boundary layer heights observed in Fig. 5 indicate that under all conditions, the random error in the mixing ratio measurement remains below 10% throughout the boundary layer at 2-min temporal and 60–200-m spatial resolution. During the daytime, the random errors increase steeply above the boundary layer where the water vapor content drops rapidly. However, under nighttime conditions, the random error does not exceed 10% below ~6 km. This analysis also indicates that during the nighttime, SRL operations with 30-m spatial resolution and 15-s temporal resolution would possess less than 10% random error up to an altitude of 3 km. These high-resolution water vapor measurements permit boundary layer convective processes to be studied throughout the diurnal cycle as further described in Demoz et al. (2006).

b. 19–20 June 2002 bore and cirrus cloud event—Upper-tropospheric measurements

In section 4a, it was demonstrated that the full utilization of the narrowband, narrow-field-of-view technique permits convective processes to be studied in the daytime boundary layer. Narrowing the spectral band and the field of view of the lidar system also enhances

upper-tropospheric water vapor measurements at night. This will now be demonstrated for the case of 19–20 June 2002, which was used for the regression analysis performed in Part I.

The extended set of SRL measurements acquired on 19–20 June 2002 revealed the atmosphere to possess a rich set of waves, or bores, in the water vapor field (Flamant et al. 2003) as indicated by the ovals on the water vapor image in Fig. 2 of Part I. The bore activity was generated by outflow from a developing thunderstorm complex that was generally to the north of the SRL location. At approximately 0630 UTC on 20 June, the strongest bore event (indicated by the oval on the lower right of the water vapor image) observed during the measurement period occurred at an altitude between 0.5 and 1.0 km. The oscillations in the moisture field at ~3.5 km, also indicated by an oval, are likely due to the upward thrust of energy from this event lower in the atmosphere. The overlying cirrus cloud field, created by anvil outflow from the thunderstorm to the north that was also the source of the bore outflow, can be seen in the aerosol scattering ratio image shown in Fig. 7. Notice that wave structure is also observed in the lower of the two scattering layers seen in this figure. Possible causes of this wave structure will be discussed later.

The potential temperature from two radiosonde launches is plotted on the figure. Radiosondes were used because of errors introduced in the rotational Raman temperature retrievals due to the cirrus particle scattering. The potential temperature is nearly constant in the intense scattering region toward the top of the upper cloud layer. Furthermore, the depth of the constant-theta region decreases in vertical extent over the measurement period while the base of the cloud lowers. This is interpreted as indicating a well-mixed cirrus anvil that is evolving into two distinct layers in terms of their dynamics and cloud microphysical properties. We hypothesize that the upper layer is a well-mixed region where previously existing ice crystals from the anvil outflow evolve and where new cirrus particles may be forming. The mean particle sizes in this upper layer are thought to be small but increase with height. The lower layer is thought to be composed of larger ice crystals that are ejected from the mixed layer. As the cirrus cloud evolves, it begins to precipitate producing the fall streaks that are present in the scattering ratio image at altitudes of 11–12 km after 2900 UTC. The generating region also decreases in vertical extent while the base of the cloud lowers. The falling ice crystals, which typically are large in size, evaporate in the dry upper troposphere and, as will be shown later, increase the relative humidity below the cloud.

1) Ice water content and particle radius retrievals

A newly developed Raman lidar technique for quantifying cirrus cloud ice water content (IWC) and generalized particle diameter (Dge) (Wang et al. 2004) makes use of simultaneous measurement of cirrus cloud scattering ratio and Raman scattering from ice. The technique was developed using measurements acquired at the U.S. Department of Energy Southern Great Plains Atmospheric Research Facility in northern Oklahoma where radar measurements were available for validation. This technique was used to retrieve IWC and particle size from these cirrus cloud measurements. The results are shown in Figs. 7c and 7d. These retrievals show that the region of intense scattering between the altitudes of 12 and 13 km and over the time interval of 0300 to 0500 UTC on 20 June (indicated as 27 and 29) is populated in general by small particles but high IWC consistent with our hypothesis of the evolution of the observed cirrus anvil. By contrast, later in the measurement period between 0800 and 1000 UTC, the retrieval of generally large particles in the 11–12-km altitude range and smaller particles above this is consistent with this being a region of cirrus precipitation.

2) Upper-troposphere humidification

To study the influence of the sublimating cirrus particles on upper-tropospheric humidity, the relative humidity with respect to ice (RH_{Ice}) was quantified at 2-h intervals during the time of the evolving cirrus cloud where temperature profiles from radiosonde were used to calculate RH_{Ice} from the lidar mixing ratio. The times at which RH_{Ice} was quantified were 0400, 0600, 0800, 1000 UTC and are indicated by the color-coded arrows in the image shown in Fig. 7b. The vertical profiles of RH_{Ice} corresponding to the times indicated by the arrows are shown in Fig. 7a. Careful study of the figure shows that subcloud RH_{Ice} values approximately double over the period of the measurements likely due to sublimation of the precipitating ice crystals from the cloud. Also observed is approximately a factor of 4 increase in the mean RH_{Ice} at the altitude of the lower scattering layer between 7 and 8 km.

3) Upper-tropospheric water vapor random error characteristics

Figure 7 demonstrates the upper-tropospheric water vapor measurement capability of the SRL during IHOP. The relative humidity profiles presented in Fig. 7 were analyzed using a routine that performs variable smoothing in both the spatial and temporal domain.

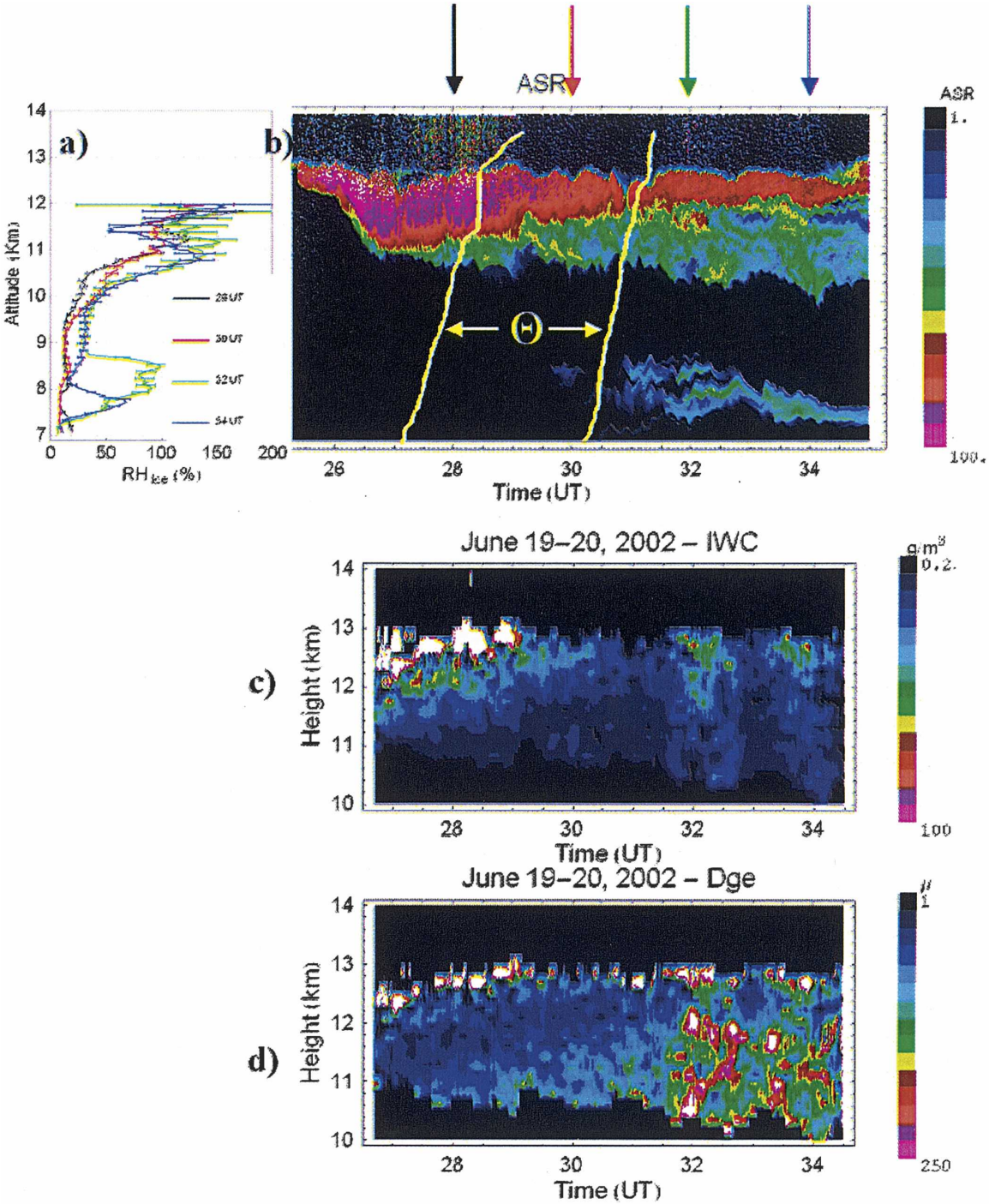

FIG. 7. (a) Relative humidity with respect to ice calculated from SRL water vapor and radiosonde temperatures at 2-h intervals during the development of the cloud system. Significant upper-tropospheric humidification is observed due to cirrus precipitation. Ice supersaturation is also observed inside the cloud. (b) Time series of aerosol scattering ratio image of a cloud system involving two layers. The upper layer is a cirrus cloud due to outflow from a thunderstorm system to the north. The lower layer, which shows interesting oscillations, is studied further in the main text. (c), (d) Ice water content and generalized particle diameter retrievals using the newly developed retrieval (Wang et al. 2004) that uses Raman scattering from ice along with the cloud scattering ratio.

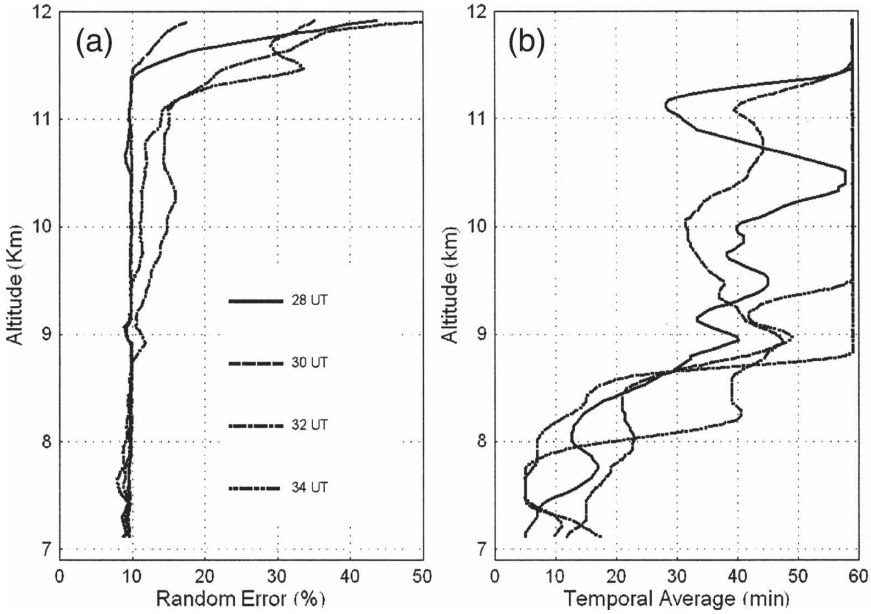

FIG. 8. (a) Random error in the relative humidity data displayed in Fig. 7. A variable smoothing routine is used that attempts to maintain less than 10% random error but does not permit more than 59 min of temporal smoothing. (b) The number of profiles used in the relative humidity profile as a function of altitude for the four profiles shown in Fig. 7.

The resulting vertical resolution of the data presented in Fig. 7 ranges from 60 m at 7 km to 600 m beyond 12 km. The procedure works as follows: the water vapor mixing ratio profiles are first vertically smoothed to the desired resolution, then the routine sums the number of profiles required to maintain the random error below a fixed value, chosen here to be 10%. At higher altitudes, more profiles are required to maintain a random error of 10% or less. A maximum number of 59 profiles, one acquired each minute, was specified for summing. This method of analyzing the data permits higher-resolution temporal features to be preserved in the lower altitudes of the profiles. On the left of Fig. 8, therefore, is shown the resulting random error as a function of altitude that is achieved using this routine. On the right is shown the number of profiles that have been included in the processed data shown in Fig. 7. Note that above some altitude, it was not possible to maintain less than 10% random error for the vertical resolution chosen. This altitude varies from ~11.5 km between 0400 and 0600 UTC to 9.5 km at 1000 UTC. The reduction in this altitude at the later times is due to the increased attenuation of the laser beam by the lower scattering layer seen in Fig. 7 between 7 and 8 km.

4) INVESTIGATION OF WAVE STRUCTURE IN LOWER SCATTERING LAYER

The oscillations in the lower scattering layer seen in Fig. 7b suggest the possibility that energy from the bore event shown at the time/altitude of ~0630 UTC/~0.5 km in the water vapor image of Fig. 2 in Part I has propagated upward to ~9 km and induced the oscillations seen in Fig. 7b. This possibility was studied by calculating the Scorer parameter, l_s^2 (Scorer 1949), which considers the balance between the atmospheric stability and wind shear as a function of altitude and can be used to identify regions of trapping for vertically propagating waves (Ralph et al. 1997; Shutts 1997). It is defined as

$$l_s^2 = \frac{N^2}{U^2} - \frac{1}{U}\frac{d^2U}{dz^2},$$

where z is the vertical coordinate, N is the Brunt–Väisälä frequency defined by

$$N^2 = \frac{g}{\theta_v}\frac{\partial\overline{\theta_v}}{\partial z},$$

and $U(z)$ is the component of the horizontal wind in the x direction. Disturbances can propagate vertically for $l_s^2 > 0$ and are trapped for $l_s^2 < 0$. The Scorer parameter calculated from radiosondes launched at 0602 and 0801 UTC (approximately 30 and 32 UTC in Fig. 7) from the Homestead site shown in Fig. 9a. The negative values of l^2 at approximately 3 km coupled with the near zero values of l^2 between 4 and 6 km do not support the hypothesis that upward-propagating energy from the bore thrust observed at 0630 UTC and 0.5 km in Fig. 2

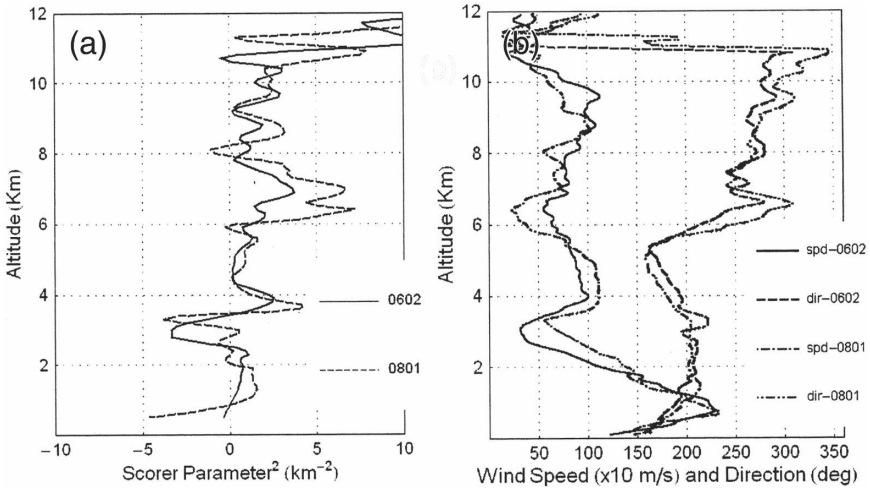

FIG. 9. (a) The Scorer parameter calculated on 20 Jun 2002 using radiosondes launched at 0602 and 0801 UTC from the Homestead site. Positive values indicate possibility of vertical propagation of waves while negative values indicate trapping of waves. (b) The wind speed and direction from the same radiosondes.

of Part I was the source of energy for the oscillations observed in the lower scattering layer in Fig. 7. Furthermore, a careful examination of the image suggests that the oscillations in the lower cloud layer may have begun prior to the major bore thrust at 0630 UTC.

To investigate other possible explanations for the presence of waves in the lower scattering layer, consider the wind speed and direction data from the 0602 and 0801 UTC radiosondes shown inFig. 9b. Large directional shear is observed in the wind field of Fig. 9 at the base of the cirrus outflow layer at ~11 km consistent with the Geostationary Operational Environmental Satellite (GOES) loop, which indicated that the outflow from the thunderstorm that produced the upper layer of cirrus clouds observed in Fig. 7 was generally from the north and then veered toward the east as the measurement period proceeded.

Within the generally westerly flow in the midtroposphere, there still was significant variation in wind direction. The wind veered continuously from approximately 160° to 300° between the altitudes of 5 and 7 km. This implies the possibility of directional shear in the wind field within this altitude range. Considering that the Scorer analysis indicates that waves can vertically propagate in the altitude range of 6–8 km and the wind analysis indicates the possibility of directional wind shear between the altitudes of 5 and 7 km, a possible explanation for the waves observed in the lower scattering layer between 7 and 9 km in Fig. 7 is that waves induced by directional wind shear have propagated vertically to the altitude of the lower scattering layer.

To further investigate the properties of the scattering layers observed in Fig. 7, the optical depth and layer mean extinction-to-backscatter ratio were calculated and are presented in Fig. 10. The optical depth of the upper cloud layer varies from a maximum of approximately 3, the rough upper limit of the SRL's ability to quantify optical depth, to approximately 1.0 between approximately 2700 and 3400 UTC (0300 and 1000 UTC on 20 June). The lower cloud layer possessed mean optical depth of approximately 0.5. Both of these values are quite consistent with cirrus clouds. However, the extinction to backscatter ratio, *S,* of the two layers is markedly different. The mean *S* value in the upper layer of ~20 sr is quite consistent with cirrus cloud values that have been measured using Raman lidar systems previously (Reichardt et al. 2002; Whiteman et al. 2004). The mean value in the lower layer of ~70–80 is quite atypical of cirrus clouds and more indicative of smoke or absorbing aerosol. The Moderate Resolution Imaging Spectroradiometer (MODIS) fire product (http://modis-fire.umd.edu/products.asp) indicated that numerous fires were present in New Mexico, Arizona, and California near the path of the 3-day back trajectories obtained from the National Oceanic and Atmospheric Administration (NOAA) Hybrid Single-Particle Lagrangian Integrated Trajectory (HYSPLIT) model (http://www.arl.noaa.gov/ready/hysplit4.html) analysis at 7, 8, and 9 km, the altitude region of the lower scattering layer seen in Fig. 7b. Therefore, we take the lower cloud layer to likely consist of hygroscopic smoke particles that have been transported from fires to the west, which have served as seeds for ice particle growth.

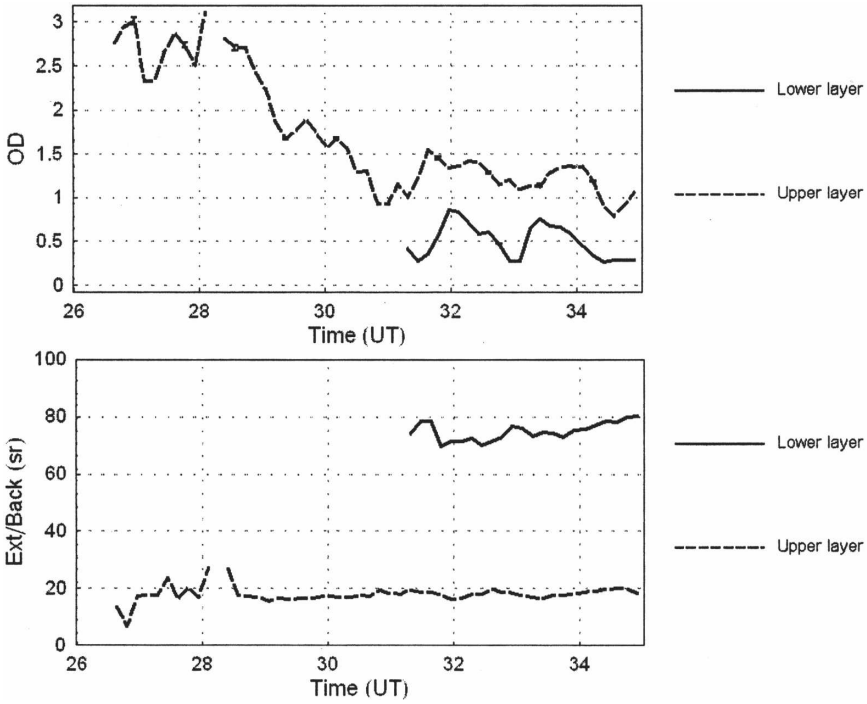

FIG. 10. (top) Layer mean optical depth and (bottom) extinction to backscatter ratio (S) for the two layers observed in Fig. 7. The S values in the upper cloud layer are quite typical for cirrus clouds; however, the much higher values in the lower layer are more consistent with smoke or dust.

There is also some indication in the lidar depolarization data that very light precipitation from the cirrus cloud may have helped to seed this lower scattering layer. Figure 11 provides both the volume and particle depolarization measurements of this cloud field. Although there is little indication of cirrus precipitation at 0300 and 0500 UTC below 10 km in the volume depolarization measurements, highly depolarizing precipitation reaching down to ~9.5 km is observed in the particle depolarization measurements. Note also that at the base of the upper cloud layer, the volume depolarization slowly rises to peak values of ~50% while the particle depolarization ratio indicates ~50% depolarization at the very base of the cloud. The particle depolarization ratio permits the depolarization properties of the particles to be separated from the molecules providing both improved contrast and more accurate characterization of the particles' scattering properties.

5) MOTIVATION OF CIRRUS CLOUD MODELING STUDY

The cirrus case of 19–20 June presented here is motivating a modeling study at NASA GSFC with the goal of understanding the physical mechanisms that produce the layering observed in the upper cloud of Fig. 7 that has been interpreted as the cirrus mixed layer (Lin et al. 2005a). The simulation of this case through numerical modeling is a considerable challenge. One hypothesis that will be investigated is that vertical differential radiative heating is the dominant effect that determines the thickness of the well-mixed layer and stabilizes the lower layer of the anvil while the cloud microphysical properties evolve accordingly. Previous studies of this type include both 1D (Khvorostyanov et al. 2001; Sassen et al. 2002; Lin et al. 2005b) and 2D (Luo et al. 2003) simulations of cloud microphysical properties, which were compared with ground-based measurements. For the case of 19–20 June, we will compare the microphysical and optical properties derived from a 2D model with multi-ice-category bin microphysics to the lidar profile measurements of ice water content, particle size, and depolarization ratio. To aid this study, the technique for reducing the cross talk between the parallel and perpendicular channels will be optimized and a multiple scattering correction will be applied to the SRL depolarization data. We will also compare the retrievals of particle size using the Raman technique described here to one based on multiple scattering in the cirrus clouds (Whiteman et al. 2001a; Gambacorta et al. 2004).

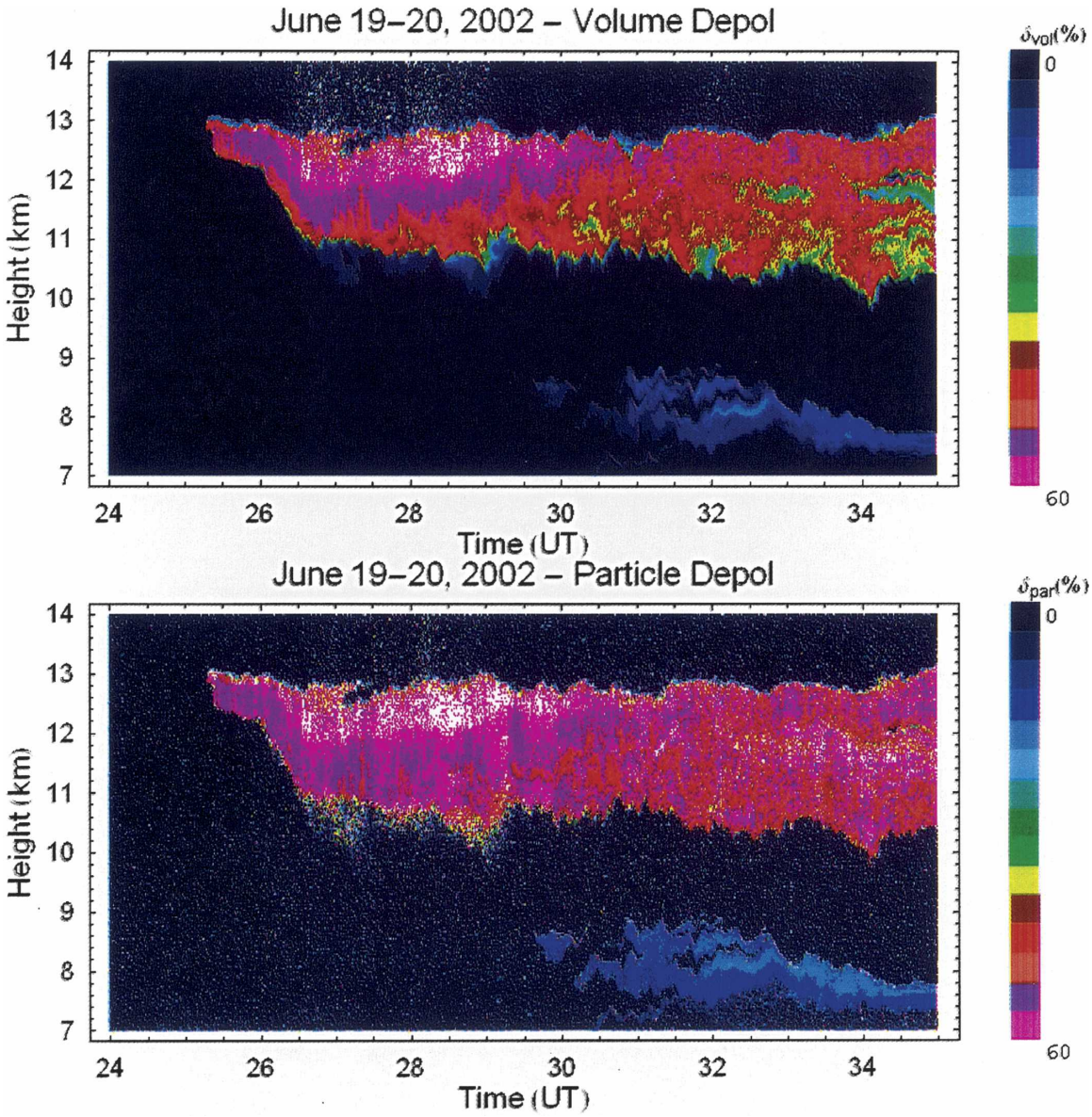

FIG. 11. (top) Volume depolarization ratio calculated for the cloud event of 19–20 Jun. (bottom) Particle depolarization ratio for the same period. The particle depolarization ratio provides a much stronger indication of cirrus precipitation at 2700 and 2900 UTC (0300 and 0500 UTC).

5. Summary

The NASA GSFC participated in the first International H_2O Project in May–June 2002. In Part I of this paper (Whiteman et al. 2006), the new SRL configuration for IHOP that included measurements of water vapor, aerosol backscatter, extinction, depolarization, liquid water, ice water, and rotational Raman temperature was described along with the analysis procedures. In Part II, comparisons of the SRL water vapor measurements and those of the LASE airborne differential absorption lidar (DIAL) water vapor lidar and the NCAR reference radiosonde were presented. Both comparisons indicated good agreement between the sensors up to an altitude of 5 km. The LASE mean precipitable water between altitudes of 0.6 and 5.0 km was 2.7% higher than the SRL value while the reference radiosonde PW was 1.5% lower than SRL. Daytime and nighttime case studies were presented to illustrate the diurnal measurement capability of the system and to quantify the random errors under these different measurement conditions. System upgrades permitted significant improvements in daytime water vapor mixing ratio measurement quality over any previous con-

figuration for a Raman lidar. In general, with effective resolution of 2 min temporally and between 60 and 210 m spatially the SRL random error remained below 10% within the boundary layer even under bright daytime conditions. The study of a convectively driven boundary layer–dryline case on 22 May demonstrated that this is sufficient resolution for convective processes to be studied. This had never been demonstrated previously using Raman lidar. The upgrades also permitted improved upper-tropospheric water vapor measurements. The upper-tropospheric measurement capability was demonstrated in the context of an evolving cirrus cloud system where humidification due to cirrus precipitation was quantified. Various other aspects of this cirrus cloud case were also studied including cirrus cloud ice water content, particle diameter, optical depth, extinction to backscatter ratio, and both volume and particle depolarization ratios. Oscillations observed in one of the cloud layers were investigated. The conclusion was that smoke particles transported from fires to the west of the measurement site likely served as ice condensation nucleii for the cloud layer. The smoke/ice particles in this layer were induced to oscillate due to vertically propagating waves created below the layer by directional wind shear. There was also some indication in the lidar particle depolarization measurements (but not in the volume depolarization measurements) that the cirrus precipitation could have helped to seed the lower cloud layer. These cirrus cloud measurements are serving to motivate cirrus cloud modeling studies.

Acknowledgments. The authors thank the NASA Interdisciplinary Program managed by Dr. Jim Dodge for its support of this activity.

REFERENCES

Browell, E. V., and S. Ismail, 1995: First lidar measurements of water vapor and aerosols from a high-altitude aircraft. *OSA Opt. Remote Sens. Atmos. Tech. Dig.,* **2,** 212–214.

——, and Coauthors, 1997: LASE validation experiment. *Advances in Atmospheric Remote Sensing with Lidar,* A. Ansmann et al., Eds., Springer-Verlag, 289–295.

Demoz, B., and Coauthors, 2006: The dryline on 22 May 2002 during IHOP_2002: Convective-scale measurements at the profiling site. *Mon. Wea. Rev.,* **134,** 293–309.

Flamant, C., and Coauthors, 2003: The life cycle of a bore event over the Southern Great Plains during IHOP_2002. Preprints, *10th Conf. on Mesoscale Processes,* Portland, OR, Amer. Meteor. Soc., CD-ROM, P2.14.

Gambacorta, A., D. N. Whiteman, Z. Wang, D. H. DeSlover, and R. M. Hoff, 2004: Particle size retrieval in cirrus clouds by use of a multiple scattering raman lidar technique. *Proc. 22d Int. Laser Radar Conf.,* Matera, Italy, European Space Agency, ESA SP-561, Vol. I, 275–278.

Khvorostyanov, V. I., J. A. Curry, J. O. Pinto, M. Shupe, B. A. Baker, and K. Sassen, 2001: Modeling with explicit spectral water and ice microphysics of a two-layer cloud system of altostratus and cirrus observed during the FIRE Arctic Clouds Experiments. *J. Geophys. Res.,* **106,** 15 099–15 112.

Lin, R.-F., D. O. Starr, J. Reichardt, and P. J. DeMott, 2005a: On the evolution of a cirrus anvil observed by NASA Scanning Raman Lidar on 19–20 June 2002 during IHOP. Preprints, *Second Symp. on Lidar Atmospheric Applications,* San Diego, CA, Amer. Meteor. Soc., CD-ROM, P2.6.

——, ——, ——, and ——, 2005b: Nucleation in synoptically forced cirrostratus. *J. Geophys. Res.,* **110,** D08208, doi:10.1029/2004JD005362.

Linné, H., D. D. Turner, J. E. M. Goldsmith, T. P. Tooman, J. Bösenberg, K. Ertel, and S. Lehmann, 2000: Intercomparison of DIAL and Raman lidar measurements of humidity profiles. *Advances in Laser Remote Sensing: Selected Papers from the 20th International Laser Radar Conference,* A. Dabas, C. Loth, and J. Pelon, Eds., Ecole Polytechnique, 293–298.

Luo, Y., S. K. Krueger, G. G. Mace, and K.-M. Xu, 2003: Cirrus cloud properties from a cloud-resolving model simulation compared to cloud radar observations. *J. Atmos. Sci.,* **60,** 510–525.

Ralph, F. M., P. Newman, T. Keller, D. Levinson, and L. Fedor, 1997: Observations, simulations, and analysis of nonstationary trapped lee waves. *J. Atmos. Sci.,* **54,** 1308–1333.

Reichardt, J., S. Reichardt, A. Behrendt, and T. J. McGee, 2002: Correlations among the optical properties of cirrus-cloud particles: Implications for spaceborne remote sensing. *Geophys. Res. Lett.,* **29,** 1668, doi:10.1029/2002GL014836.

Sabatino, D., and Coauthors, 2004: Water vapour measurements during the International H_2O Project: Intercomparisons between Scanning Raman Lidar and LASE. *Proc. 22d Int. Laser Radar Conf.,* Matera, Italy, European Space Agency, ESA SP-561, Vol. I, 435–438.

Sassen, K., Z. Wang, V. I. Khvorostyanov, G. L. Stephens, and A. Bennedetti, 2002: Cirrus cloud ice water content radar algorithm evaluation using an explicit cloud microphyhsical model. *J. Appl. Meteor.,* **41,** 620–628.

Scorer, R. S., 1949: Theory of waves in the lee of mountains. *Quart. J. Roy. Meteor. Soc.,* **75,** 41–56.

Senff, C., J. Bösenberg, and G. Peters, 1994: Mesurement of water vapor flux profiles in the convective boundary layer with lidar and RADAR–RASS. *J. Atmos. Oceanic Technol.,* **11,** 85–93.

Shutts, G., 1997: Operational lee wave forecasting. *Meteor. Appl.,* **4,** 23–35.

Wang, J., D. J. Carlson, D. B. Parsons, T. F. Hock, D. Lauritsen, H. L. Cole, K. Beierle, and E. Chamberlain, 2003: Performance of operational radiosonde humidity sensors in direct comparison with a chilled mirror dew-point hygrometer and its climate implication. *Geophys. Res. Lett.,* **30,** 1860, doi:10.1029/2003GL016985.

Wang, Z., D. N. Whiteman, B. B. Demoz, and I. Veselovskii, 2004: A new way to measure cirrus cloud ice water content by using ice Raman scatter with Raman lidar. *Geophys. Res. Lett.,* **31,** L15101, doi:10.1029/2004GL020004.

Weckworth, T. M., and Coauthors, 2004: An overview of the In-

ternational H_2O Project (IHOP_2002) and some preliminary highlights. *Bull. Amer. Meteor. Soc.,* **85,** 253–277.

Whiteman, D. N., S. H. Melfi, and R. A. Ferrare, 1992: Raman lidar system for the measurement of water vapor and aerosols in the earth's atmosphere. *Appl. Opt.,* **31,** 3068–3082.

——, and Coauthors, 2001a: Raman lidar measurements of water vapor and cirrus clouds during the passage of hurricane Bonnie. *J. Geophys. Res.,* **106** (D6), 5211–5225.

——, G. Schwemmer, T. Berkoff, H. Plotkin, L. Ramos-Izquierdo, and G. Pappalardo, 2001b: Performance modeling of an airborne Raman water vapor lidar. *Appl. Opt.,* **40,** 375–390.

——, Z. Wang, and B. Demoz, 2004: Subtropical cirrus cloud extinction to backscatter ratios measured by Raman lidar during CAMEX-3. *Geophys. Res. Lett.,* **31,** L12105, doi:10.1029/2004GL020003.

——, and Coauthors, 2006: Raman water vapor lidar measurements during the International H_2O Project. Part I: Instrumentation and analysis techniques. *J. Atmos. Oceanic Technol.,* **23,** 157–169.